Neurobiology of Disease

Reactivation of Lysosomal Ca^{2+} Efflux Rescues Abnormal Lysosomal Storage in FIG4-Deficient Cells

Jianlong Zou,[1,2]* Bo Hu,[2]* Sezgi Arpag,[2] Qing Yan,[2] Audra Hamilton,[2] Yuan-Shan Zeng,[1] Carlos G. Vanoye,[3] and Jun Li[2,4]

[1]Department of Histology and Embryology, Zhongshan School of Medicine, Sun Yat-sen University, Guangzhou 510085, China, [2]Department of Neurology, Center for Human Genetics Research, Vanderbilt Brain Institute, Vanderbilt University School of Medicine, Nashville, Tennessee 37232, [3]Department of Pharmacology, Northwestern University, Evanston, Illinois 60208, and [4]Tennessee Valley Healthcare System–Nashville Veterans Administration, Nashville, Tennessee 37212

Loss of function of FIG4 leads to Charcot-Marie-Tooth disease Type 4J, Yunis-Varon syndrome, or an epilepsy syndrome. FIG4 is a phosphatase with its catalytic specificity toward 5′-phosphate of phosphatidylinositol-3,5-diphosphate ($PI3,5P_2$). However, the loss of FIG4 decreases $PI3,5P_2$ levels likely due to FIG4's dominant effect in scaffolding a $PI3,5P_2$ synthetic protein complex. At the cellular level, all these diseases share similar pathology with abnormal lysosomal storage and neuronal degeneration. Mice with no FIG4 expression (*Fig4*$^{-/-}$) recapitulate the pathology in humans with FIG4 deficiency. Using a flow cytometry technique that rapidly quantifies lysosome sizes, we detected an impaired lysosomal fission, but normal fusion, in *Fig4*$^{-/-}$ cells. The fission defect was associated with a robust increase of intralysosomal Ca^{2+} in *Fig4*$^{-/-}$ cells, including FIG4-deficient neurons. This finding was consistent with a suppressed Ca^{2+} efflux of lysosomes because the endogenous ligand of lysosomal Ca^{2+} channel TRPML1 is $PI3,5P_2$ that is deficient in *Fig4*$^{-/-}$ cells. We reactivated the TRPML1 channels by application of TRPML1 synthetic ligand, ML-SA1. This treatment reduced the intralysosomal Ca^{2+} level and rescued abnormal lysosomal storage in *Fig4*$^{-/-}$ culture cells and *ex vivo* DRGs. Furthermore, we found that the suppressed Ca^{2+} efflux in *Fig4*$^{-/-}$ culture cells and *Fig4*$^{-/-}$ mouse brains profoundly downregulated the expression/activity of dynamin-1, a GTPase known to scissor organelle membranes during fission. This downregulation made dynamin-1 unavailable for lysosomal fission. Together, our study revealed a novel mechanism explaining abnormal lysosomal storage in FIG4 deficiency. Synthetic ligands of the TRPML1 may become a potential therapy against diseases with FIG4 deficiency.

Key words: **Charcot-Marie-Tooth disease; lysosomal storage; membrane trafficking; ML-SA1; neurodegeneration; TRPML1**

Introduction

Autosomal recessive mutations in the *FIG4* gene cause three distinct neurological disorders: Charcot-Marie-Tooth disease Type 4J (CMT4J) with neuronal degeneration in the peripheral nervous system (Chow et al., 2007; Zhang et al., 2008; Nicholson et al., 2011), Yunis–Varon syndrome with mental retardation and cleidocranial dysplasia (Campeau et al., 2013), and seizures with cerebral polymicrogyria. *FIG4* encodes a phosphatase with its catalytic specificity toward the 5′-phosphate of phosphatidylinositol-(3,5)-bisphosphate ($PI3,5P_2$). FIG4 (SAC3 in mammalian cells) complexes with a scaffolding protein Vac14 (=ArPIKfyve) and a 5′-kinase of PI3P known as Fab1 (PIKfyve) (Jin et al., 2008; Ikonomov et al., 2009). This PAS complex mediates the conversion of early endosomal PI3P to late endosomal $PI3,5P_2$ (Sbrissa et al., 2007; Huotari and Helenius, 2011). In this manner, FIG4 can decrease $PI3,5P_2$ levels via its phosphatase action and also promote $PI3,5P_2$ synthesis by acting as a secondary scaffold for the Fab1/Vac14 interaction. However, the latter function appears to be dominant as loss of FIG4 in *Fig4*$^{-/-}$ mice results in a reduction of $PI3,5P_2$ (Chow et al., 2007).

Mice with homozygous truncation mutations in *Fig4* (also called *pale tremor* = *Fig4*$^{-/-}$) recapitulate the pathology seen in humans with FIG4 deficiency (Chow et al., 2007; Zhang et al., 2008; Katona et al., 2011). At the cellular level, all these diseases and *Fig4*$^{-/-}$ mice share a common feature: abnormal lysosomal storage (Walch et al., 2000; Katona et al., 2011; Martyn and Li, 2013). Although mechanisms leading to the lysosomal storage are unclear, excessive lysosomal storage in these diseases is consistent with the documented role of $PI3,5P_2$ in endolysosomal membrane trafficking. This lysosomal storage is not related to abnormal autophagy (Katona et al., 2011; Ferguson et al., 2012; Martyn

Received Oct. 15, 2014; revised March 18, 2015; accepted March 22, 2015.

Author contributions: J.Z. and J.L. designed research; J.Z., B.H., S.A., A.H., C.G.V., and Q.Y. performed research; J.L. contributed unpublished reagents/analytic tools; J.Z., B.H., Y.-S.Z., C.G.V., J.L., and Q.Y. analyzed data; J.Z. and J.L. wrote the paper.

J.Z. is a PhD candidate who has been supported by Natural Science Foundation of China (81129019). This work was supported by National Institute of Neurological Disorders and Stroke Grants R01NS066927 and R21NS081364 to J.L. and Department of Veterans Affairs Research and Development funds to J.L. We thank the Vanderbilt Flow Cytometry Shared Resource and Vanderbilt Cell Imaging Shared Resource for technical support; and Dr. Lily Wang (Department of Biostatistics, Vanderbilt University) for assistance in our statistical analysis.

The authors declare no competing financial interests.

*J.Z. and B.H. contributed equally to this work.

Correspondence should be addressed to Dr. Jun Li, Department of Neurology, Vanderbilt University School of Medicine, 1161 21st Avenue South, Nashville, TN 37232. E-mail: jun.li.2@vanderbilt.edu.

Q. Yan's present address: Shenyang Normal University, 253 Huanghe N Street, Yuhong, Shenyang, Liaoning, China.

DOI:10.1523/JNEUROSCI.4442-14.2015

 0270-6474/15/356801-12$15.00/0

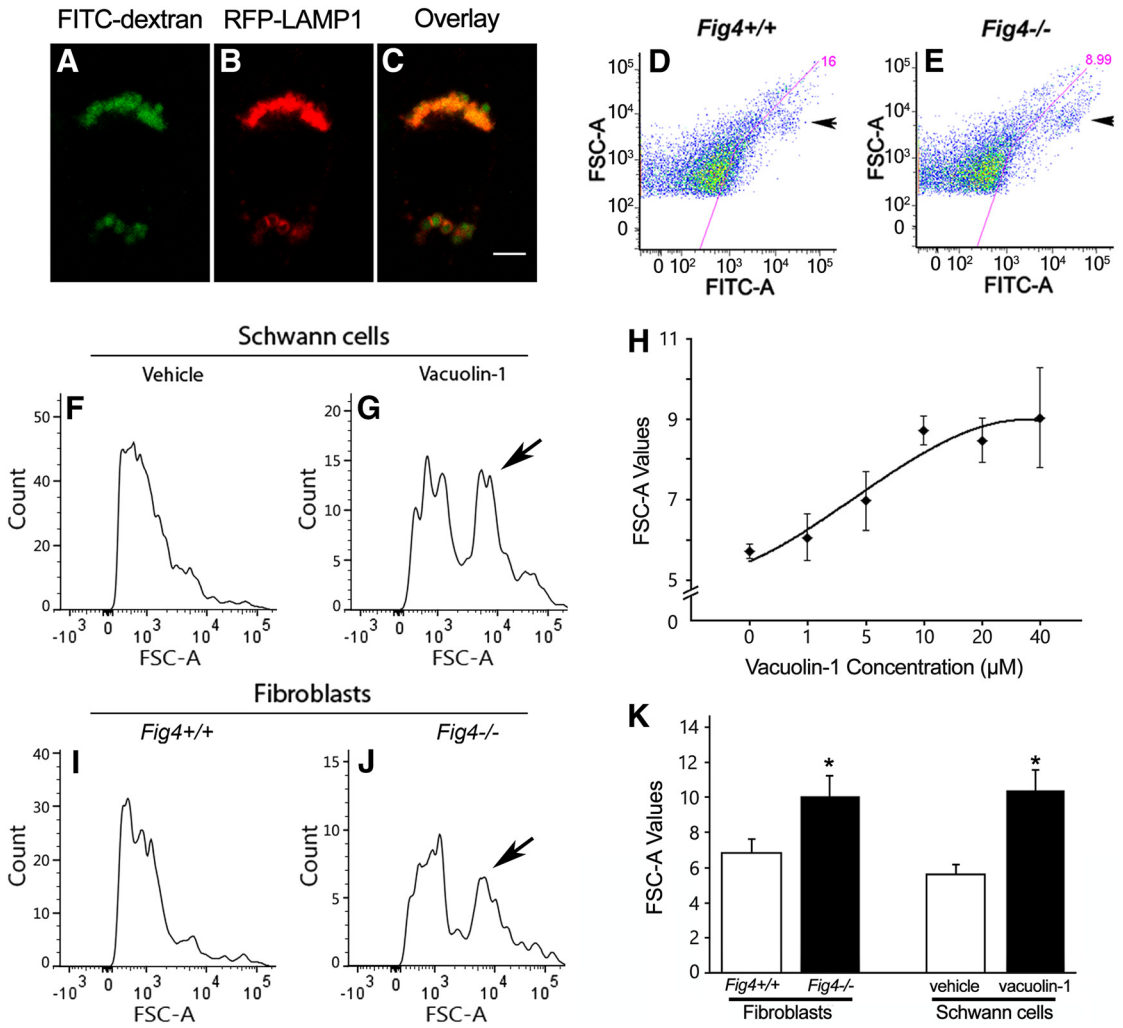

Figure 1. Establishment of an automated quantification of lysosome sizes. ***A–C***, RT4 rat Schwann cell line was preloaded with FITC-dextran at the concentration of 5 μg/ml and transfected with RFP-LAMP1 vector, cultured overnight, and followed by a 45 min chase. FITC-dextran specifically labeled the lysosomes of Schwann cells. Scale bar, 5 μm. ***D***, ***E***, The FITC-dextran fluorescence allowed the flow cytometry to isolate lysosomes, whose sizes were quantified by laser-beam FSC-A values. FSC-A values from mouse *Fig4*$^{-/-}$ fibroblasts were larger than that in mouse *Fig4*$^{+/+}$ fibroblasts (arrows). ***F***, ***G***, ***I***, ***J***, Lysosome size distribution is illustrated in a histogram. Vehicle-treated RT4-Schwann cells (***F***) and *Fig4*$^{+/+}$ fibroblasts (***I***) showed a single peak of FSC-A values. In contrast, vacuolin-1 (5 μM/L)-treated Schwann cells (***G***) and *Fig4*$^{-/-}$ fibroblasts (***J***) developed another peak toward larger FSC-A values (arrow). ***H***, RT4-Schwann cells were treated with different concentrations of vacuolin-1 for 45 min. Dose-dependent curve shows that the lysosome sizes increased along with the increase of vacuolin-1 concentrations. ***K***, Histogram shows the comparison of lysosome sizes between different experimental groups. The flow cytometry detected a significant increase of lysosome sizes (FSC-A values) in either vacuolin-1-treated cells or *Fig4*$^{-/-}$ mouse fibroblasts. Error (vertical) bars indicate SD, which also applies to all other figures in this paper. Asterisks (*) indicate statistically significant.

and Li, 2013). Therefore, unlike canonical lysosomal storage diseases with deficiency of enzymatic degradation, FIG4 deficiency affects a different aspect of lysosomal function, namely, membrane trafficking.

Lysosome size is dynamically regulated by lysosomal membrane fusion and fission (Durchfort et al., 2012). Equilibrium of the two processes would have to be tightly controlled to maintain proper lysosomal size. Molecular machinery executing fusion is relatively better understood. It initiates with tethering two vesicular membranes that require Rab GTPases. Rab recruits additional bridging proteins, such as the homotypic fusion and protein sorting complex or Vamp7, which promote a mixing of lipid bilayers for fusion (Luzio et al., 2007). In contrast, lysosomal fission is minimally explored. In the present study, we demonstrated an impaired lysosomal fission, but not fusion, in *Fig4*$^{-/-}$ cells. Moreover, we found that this fission defect is related to a robust increase of intralysosomal Ca^{2+} level in *Fig4*$^{-/-}$ cells. Release of the Ca^{2+} from *Fig4*$^{-/-}$ lysosomes rescued abnormal lysosomal storage.

Materials and Methods

Mouse genotyping, skin biopsies to culture fibroblasts, and production of conditionally immortalized Schwann cells. The *Fig4*$^{-/-}$ mice were genotyped as described previously (Chow et al., 2007). Both males and females were used and matched between different experimental groups. Skin biopsies from *Fig4*$^{+/+}$ and *Fig4*$^{-/-}$ mice were transferred to culture dishes. The tissues were submerged in DMEM (including 10% FBS and 1× penicillin/streptomycin) for fibroblast culture that will be detailed below.

The primary Schwann cell culture is time-consuming. We expected a large amount of Schwann cells needed in this and subsequent studies. We thus prepared conditionally immortalized Schwann cells. The property of primary cells was largely preserved in these immortalized cells (Cárdenas et al., 2002; Saavedra et al., 2008). *Fig4*$^{+/-}$ mice were crossed with *SV40* transgenic mice (*SV40tg*; from The Jackson Laboratory) to produce *Fig4*$^{+/-}$*/SV40tg* mice. At postnatal day 5 (P5), sciatic nerves were dissected and Schwann cells were cultured at 33°C. This low temperature activated *SV40tg*, which promoted cell proliferation to a large quantity (Cárdenas et al., 2002; Saavedra et al., 2008). Cells were allowed to differentiate by transferring them to a 37°C, which inactivated *SV40tg* and

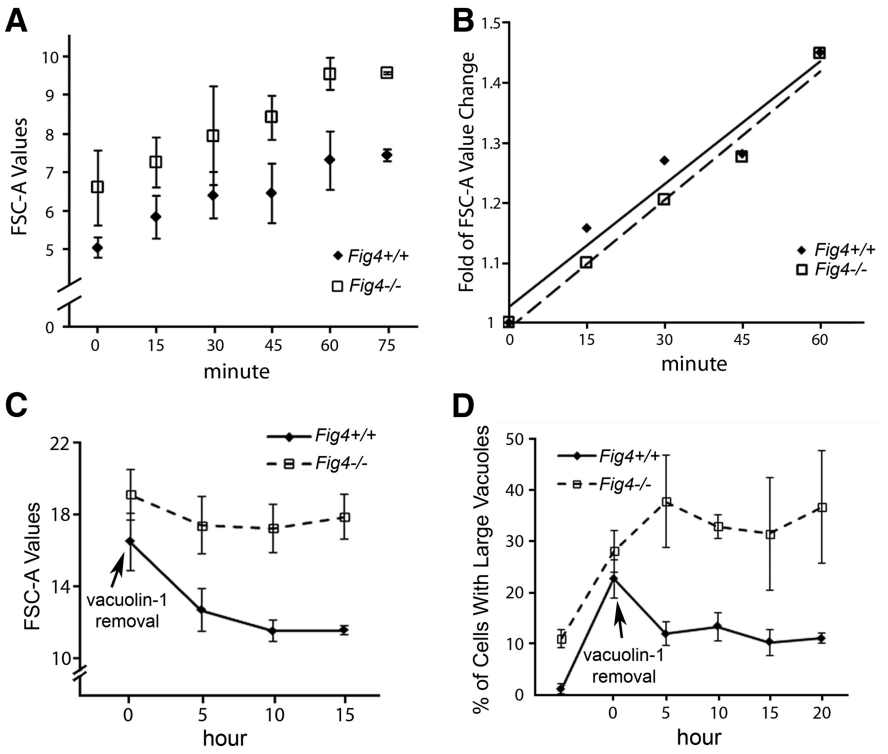

Figure 2. Evaluation of lysosomal fusion and fission. ***A***, ***B***, Mouse fibroblasts were incubated with Acetate Ringer's medium for 30 min to fragment lysosomes. After the Ringer's medium was removed, the lysosome size was quantified by the flow cytometry. There was no significant difference in the rate of lysosome-size increase between *Fig4* $^{+/+}$ and *Fig4* $^{-/-}$ fibroblasts. ***C***, ***D***, Fibroblasts were treated with vacuolin-1 (5 μM) to increase lysosome sizes. ***C***, After removal of vacuolin-1, lysosome sizes were measured by flow cytometry at different time points. By the 15th hour, the size of lysosomes reached 83 $\pm$ 12% recovery in *Fig4* $^{+/+}$ cells, compared with 37 $\pm$ 9% recovery in *Fig4* $^{-/-}$ cells ($p < 0.01$; $n = 5$). ***D***, We manually quantified percentages of cells that contained more than one lysosome with size larger than one-third of the nuclear diameter. After the removal of vacuolin-1, a strong recovery was observed in *Fig4* $^{+/+}$ fibroblasts; however, these large lysosomes in *Fig4* $^{-/-}$ cells were further enlarged and showed no recovery. The statistical significance was found at time point 5 and 10 h.

restored the primary property of these cells. Identity of Schwann cells was confirmed by staining the cells with S100 antibodies. *Fig4* $^{-/-}$*/SV40tg* Schwann cells developed vacuoles, which were indistinguishable from those described in the original *Fig4* $^{-/-}$ fibroblasts (Chow et al., 2007; Zhang et al., 2008) (data not shown).

Cell culture and lysosomal labeling. Rat Schwann cell-line (RT4) was purchased from (ATCC CRL-2768). Fibroblasts were isolated from *Fig4* $^{+/+}$ and *Fig4* $^{-/-}$ mouse skin biopsies. Cells were seeded on 6-well plates and cultured in DMEM, supplemented with 10% FBS. Cells were incubated with FITC-dextran (5 μg/ml; D-3305, Invitrogen) overnight followed by 2 h chasing to label lysosomes. Acetate Ringer's medium (to fragment lysosomes) contained 80 mM NaCl, 70 mM sodium acetate, 5 mM KCl, 2 mM $CaCl_2$, 1 mM $MgCl_2$, 2 mM NaH_2PO_4, 10 mM HEPES, 10 mM glucose, and 0.5 mg/ml BSA.

Isolation of intracellular organelles. Fibroblasts in 6-well plates grown until 80% confluence, followed by incubation with FITC-dextran to label lysosomes. Cells were washed twice with 4°C DMEM-no Phenol Red (Invitrogen) and transferred into 4°C FACS loading buffer (275 mM sucrose, 20 mM HEPES, pH 7.2, 1 mM EGTA). Cytoplasmic membranes were ruptured using a Dunce homogenizer (Kimble/Kontes; #885303-0002) to stroke up and down 20 times. Homogenates were centrifuged at 400 $\times$ *g* for 4 min to collect intracellular organelles from supernatants (Perou et al., 1997). Unruptured cells or nuclei were removed during centrifugation.

Flow cytometry. Organelles were placed in a 5 ml polystyrene tube (BD Falcon; #352058) for cytometry on BD-LSRII at Vanderbilt Flow Cytometry Core. The analysis was done using software BD FACSDiva version 6.1.3 and Flowjo version 10. A sample of unlabeled organelles was used to set a background for isolation of the FITC-dextran-labeled lysosomes. Because a fraction of lysosomes were large in size, the upper limit of forward scatter area (FSC-A) values (representing organelle size) was open to include all large organelles. Nuclei and unruptured cells were removed by centrifugation. Multiple organelles could cluster into a single large particle. These particles were excluded by setting up an additional discrimination window based on BD FACService TechNotes (BD 9:4; October, 2004). Typically, there were 10,000 events collected for each sample. To reduce variations between experiments, each measurement was performed with a standard sample of liposomes with a diameter of 400 nm. All FSC-A values were normalized by the FSC-A value of the 400 nm liposomes.

Confocal imaging. Schwann cells, fibroblasts, or neurons were cultured on 35 mm glass-bottom dishes (In Vitro Scientific; #D35-14-1.5-N). Cells were preloaded with the FITC-Dextran and/or transfected with red fluorescence protein (RFP)-LAMP1 vector (CellLight Lysosomes-RFP, BacMam 2.0; Molecular Probes) and grown overnight. Fluorescence was imaged under a Zeiss LSM510 confocal microscopy at Vanderbilt Imaging Core.

For measuring Ca^{2+} levels, we used two different dyes: Calcium Orange (4 μM, Molecular Probes; #C3015) or Oregon Green (10 μM; Molecular Probes; catalog #06809). The cells were then stained with Calcium Orange for 45 min or Oregon Green for 2.5 h before the dye was removed. Cells were incubated for another 2 h to allow the Oregon Green to enter the intracellular organelles before imaging. Calcium Orange was imaged right after the dye was washed out with nonphenol red DMEM.

Ex vivo *preparation of DRG.* Spinal cord segments with attached DRGs were dissected from P5 *Fig4* $^{-/-}$ mice. Each segment was cut in a half at the mid-line with one-half for vehicle and the other for ML-SA1 (40 μM) treatment for 36 h incubation in neurobasal media. The tissues were then fixed in 4% PFA for 24 h before being embedded into paraffin blocks. Paraffin sections were stained with cresyl violet (0.2% in acetate buffer) for 1–2 min, rinsed in 70% ethanol, and followed by nucleus staining with DAPI. Under fluorescent microscopy, DRG neuronal cell body was visualized through the autofluorescence of cresyl violet. Intracellular vacuoles with a diameter $\geq$2 μm were readily detectable due to the absence of autofluorescence. We counted percentages of neurons with vacuoles (diameters $\geq$2 μm) as described previously (Katona et al., 2011).

Morphological analysis of lysosomal vacuoles. In a subset of fibroblast culture experiments, lysosome size was quantified manually under a 63$\times$ objective lens. We imaged five predefined fields on each slide. Images were imported into ImageJ. The areas of each field were measured. Within each field, we counted fibroblasts with large lysosomal vacuoles that had their diameters more than one-third of the nuclear diameter.

GTPase activity assay. This method was modified from a previous publication (Zhang et al., 2013). Cells were washed twice with ice-cold PBS and lysed in 0.3 ml buffer (Mg^{2+} lysis/wash buffer + 1$\times$ protease inhibitor mixture) and centrifugation at 13,000 $\times$ *g* for 5 min. Supernatant were incubated with 0.25 volume of GTP-agarose (Sigma; G9768) overnight at 4°C on a rotator. Beads were washed and centrifuged in the lysis buffers. GTP-binding proteins were eluted with an equal volume of elution buffer (5–10 mM GTPγS in the lysis buffer) for 2 h at 4°C. The supernatant was subjected to Western blot.

Western blot. Cells were lysed in RIPA buffer (#R0278, Sigma) with proteinase/phosphatase inhibitor mixture (#5872S, Cell Signaling Tech-

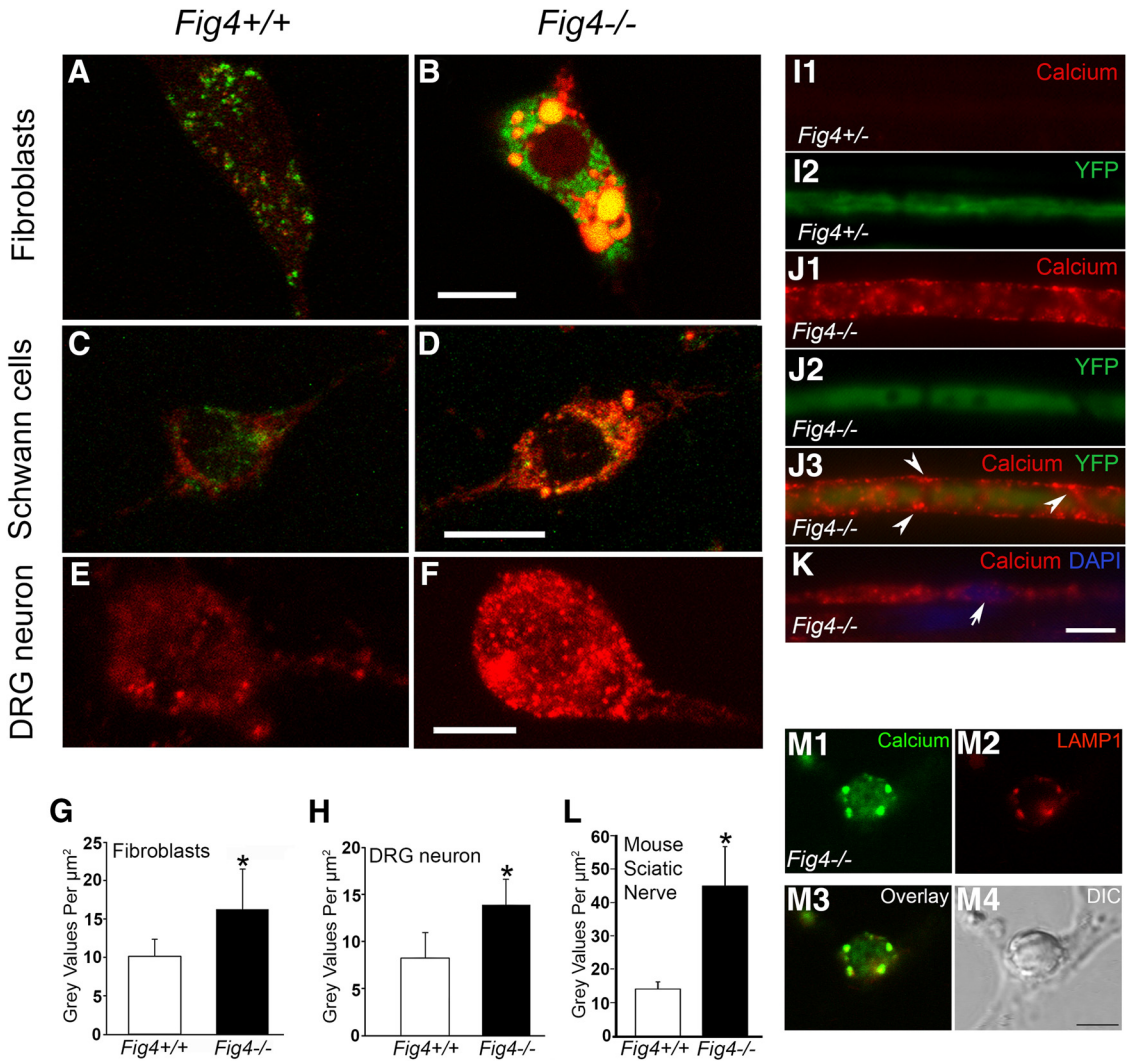

Figure 3. High Ca^{2+} level in *Fig4* $^{-/-}$ lysosomes. The FITC-dextran (green) labeled fibroblasts (***A***, ***B***), mouse conditionally immortalized Schwann cells (***C***, ***D***), and primary DRG neuron (***E***, ***F***) were costained with a Ca^{2+}-dye Calcium Orange (4 μM, Molecular Probes; #C3015; red) for 45 min, during which the dye reached the intracellular organelles. After washing the dye out with nonphenol red DMEM, confocal images showed Ca^{2+} fluorescence intensity was higher in *Fig4* $^{-/-}$ cells than that in *Fig4* $^{+/+}$ fibroblasts. A similar increase of Ca^{2+} level was observed in the immortalized Schwann cells and primary DRG neurons. The Ca^{2+} signals were colocalized with lysosomal marker FITC-dextran (yellow). ***G***, This intensity of Ca^{2+} fluorescence in fibroblasts was quantified. There was a significantly increased Ca^{2+} level in *Fig4* $^{-/-}$ fibroblasts, compared with that in *Fig4* $^{+/+}$ fibroblasts (10 wells with a total of 156 *Fig4* $^{+/+}$ cells and 10 wells with a total of 156 *Fig4* $^{-/-}$ cells; $p < 0.01$). * ***H***, The Ca^{2+} level in *Fig4* $^{-/-}$ DRG neuron was also higher than that in *Fig4* $^{+/+}$ DRG neuron (4 wells with a total of 53 *Fig4* $^{+/+}$ cells and 4 wells with a total of 20 *Fig4* $^{-/-}$ cells; $p < 0.01$). ***I1***, Ca^{2+} levels were measured by preloading Calcium Orange-1-AM into mouse sciatic nerve myelin. Methods for measuring Ca^{2+} level were detailed by Yan et al. (2010). The Ca^{2+} signal was minimal in *Fig4* $^{+/-}$ and *Fig4* $^{+/+}$ mouse nerves. ***I2***, The presence of nerve fibers was verified by YFP-labeled axons. ***J1***, ***J2***, The Ca^{2+} signals were strong in *Fig4* $^{-/-}$ nerves. ***J3***, The increased Ca^{2+} signals (arrowheads) in *Fig4* $^{-/-}$ myelinated nerve appeared to be in myelin, presumably in internodal Cajal tunnels. ***K***, Another nerve fiber showed the Ca^{2+} increase around the Schwann cell perinuclear region (nucleus is pointed by an arrow). ***L***, Quantification of Ca^{2+} fluorescence intensity (Leica; FM6000B) confirmed a significant difference between *Fig4* $^{+/+}$ and *Fig4* $^{-/-}$ mice ($n = 3$ mice for each group; 30 myelinated nerve fibers from each mouse were measured; $p < 0.05$). ***M***, Conditionally immortalized *Fig4* $^{-/-}$ Schwann cells were transfected with the BacMam vector 2.0 (Invitrogen; catalog #C10597) expressing an RFP-fused LAMP1, a lysosomal transmembrane protein. These cells were then double-stained with a calcium dye, Oregon Green. ***M1***, Ca^{2+} fluorescence was evident in a large lysosomal vacuole. ***M2***, The enlarged lysosome was demarcated by the lysosomal membrane protein LAMP1. ***M3***, A superimposed image of LAMP1 and Ca^{2+} dye. ***M4***, A phase-contrast image revealed the overall size and position of the lysosomal vacuole in the Schwann cell. Scale bar, 5 μm. Asterisks (*) indicate statistically significant.

nology). The protein concentration was determined by BCA protein assay (#23225, Thermo Scientific). The protein sample was loaded into SDS-polyacrylamide gel. The remaining steps were similar to what we described (Katona et al., 2011).

Patch-clamp recording on Fig4 $^{+/+}$ *and* Fig4 $^{-/-}$ *Schwann cells.* Conditionally immortalized Schwann cells were dissociated by brief exposure to trypsin, plated on glass coverslips, and allowed to recover for ~1 h at 37°C in 5% CO_2. Whole-cell currents were recorded at room temperature (20°C–23°C) using Axopatch 200B amplifiers (Molecular Devices) in the whole-cell configuration of the patch-clamp technique (Hamill et al., 1981). Pulse generation was performed via Clampex 8.0 (Molecular Devices) and whole-cell currents were filtered at 1 kHz and acquired at 5 kHz. The access resistance and apparent membrane capacitance were estimated using an established method (Lindau and Neher, 1988). Whole-cell currents were not leak-subtracted. Whole-cell currents were measured from −80 to 60 mV (in 20 mV steps) from a holding potential of 0 mV. We used solutions similar to those previously used (Mignen and Shuttleworth, 2001). The control external solution contained (in mM) the following: NaCl 140, $MgCl_2$ 1.2, $CaCl_2$ 20, glucose 10, HEPES 10, pH 7.4. The divalent-fee external solution contained the following (in mM): NaCl 140, glucose 10, HEPES 10, sucrose 30, pH 7.4. The internal solution contained the following (in mM): CsOH 140, aspartic acid 140, $MgCl_2$ 1.22, EGTA 5, HEPES 10, pH 7.2. Pipette solution was diluted 5%–10% to prevent activation of swelling-activated currents. Patch pi-

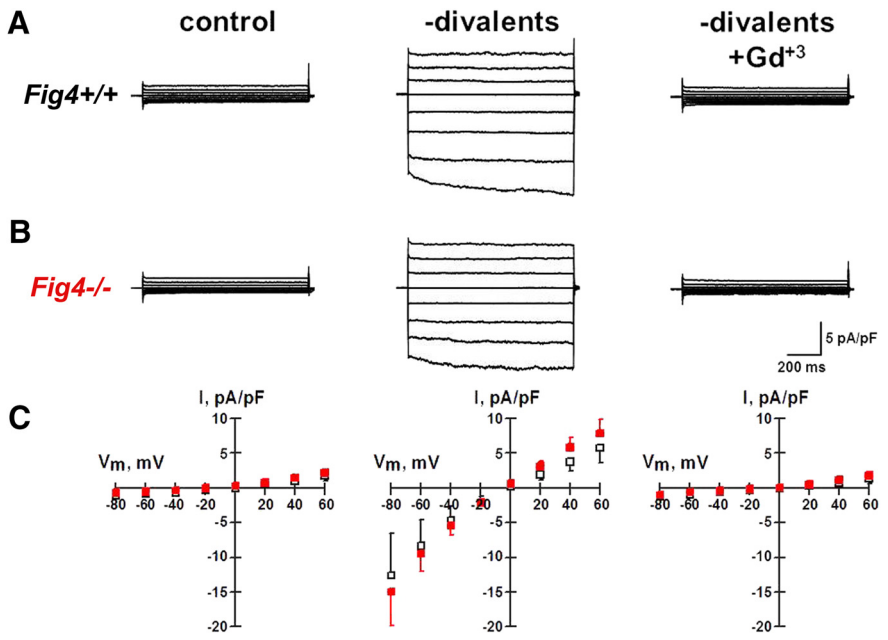

Figure 4. The increase of intralysosomal Ca^{+2} is unlikely from extracellular sources. ***A–C***, Whole-cell currents from *Fig4* $^{+/+}$ and *Fig4* $^{-/-}$ conditionally immortalized Schwann cells were recorded by patch-clamp technique in control and divalent free ($-Ca^{+2}/Mg^{+2}$, DVF) solutions. Following passive depletion of ER stores, removal of external divalent cations (middle) generated similar currents in both cell populations. These currents were blocked by external gadolinium (Gd^{+3}, 10 μM, right). Bottom, Average current voltage relationships normalized for membrane capacitance, measured from *Fig4* $^{+/+}$ (□, $n = 8$) and *Fig4* $^{-/-}$ (■, $n = 10$) cells exposed to control (***A–C***, left column). DVF (***A–C***, middle column) and DVF + Gd^{+3} (***A–C***, right column) external solutions. Studies in HEK293 cells indicate that currents with similar properties (activation by passive depletion of ER calcium stores and removal of external Ca^{+2} and Mg^{+2} and blocked by Gd^{+3}) are carried by store-operated Ca^{2+} channels (Mignen and Shuttleworth, 2001).

pettes were pulled from thick-wall borosilicate glass (World Precision Instruments) with a multistage P-97 Flaming-Brown micropipette puller (Sutter Instruments) and heat-polished with a Microforge MF 830. After heat polishing, the resistance of the patch pipettes was 3–5 MΩ in the standard extracellular solution. The access resistance varied from 5 to 9 MΩ. As a reference electrode, a 2% agar-bridge with composition similar to the control bath solution was used. Junction potentials were zeroed with the filled pipette in the bath solution. Data were analyzed and plotted using a combination of Clampfit (Molecular Devices) and SigmaPlot 2000 (Systat Software). Whole-cell currents are normalized for membrane capacitance, and results are expressed as mean ± SEM.

Statistics. We compared continuous variables between two groups using Student's *t* test. The difference among more than two groups was compared using one-way ANOVA if data were under normal distribution or Wilcoxon Mann–Whitney Test if data were not under normal distribution. *p* values of <0.05 indicated a statistical significance. Exceptions are listed below.

For Figure 2*A*, to compare slopes of changes over time for the two groups, we used a linear regression model with normalized FSC-A values as the outcome variable and group, time, and group × time as independent variables. Parameters from this model were estimated and then compared with test if the slopes were equal for the two groups. For Figure 2*B*, the same model was used, except by replacing outcome variable with fold of FSC-A value changes. The null hypothesis was H0: slope for *Fig4* $^{+/+}$ = slope for *Fig4* $^{-/-}$ group. The slopes for the two groups were similar and showed no evidence to reject null hypothesis ($p > 0.05$). For Figure 2*C*, *D*, we compared the change values from baseline (or vehicle) between the two groups using Wilcoxon Rank-sum test. Exact *p* values were calculated because of the small sample sizes.

Results

Establishment of an automated quantification system for lysosome sizes

To quantitatively examine the fission of lysosomes, we established an automated technique that can rapidly measure the lysosome sizes by modifying a reported method (Durchfort et al., 2012) (Fig. 1). The method is detailed in Materials and Methods, including lysosomal labeling with FITC-conjugated dextran, intracellular organelle isolation, and flow cytometry analysis.

The RT4 Schwann cell line was treated with vacuolin-1 (5 μM/L), a reagent known to enlarge lysosomes by an unknown mechanism (Cerny et al., 2004). There was a significant increase of lysosomal sizes in vacuolin-1-treated cells (10.4 ± 1.2 FSC-A values; $n = 12$ cultures) compared with that in the vehicle-treated cells (5.6 ± 0.6; $n = 11$; $p < 0.01$; Fig. 1*F*,*G*,*K*). The increases of lysosomal sizes by vacuolin-1 were dose-dependent (Fig. 1*H*). Moreover, this experiment revealed significantly increased lysosome sizes in *Fig4* $^{-/-}$ mouse fibroblasts (10.1 ± 1.2; $n = 6$ cultures), compared with those of *Fig4* $^{+/+}$ fibroblasts (6.8 ± 0.8; $n = 8$; $p < 0.01$; Fig. 1*I–K*). Therefore, this method is reliable, rapid, and can quantify thousands of lysosomes within a minute.

Lysosomal fission, but not fusion, is decreased in *Fig4* $^{-/-}$ cells

Next, we tested whether there is an altered balance between lysosomal fusion and fission in *Fig4* $^{-/-}$ cells. Mouse fibroblasts were incubated with Acetate Ringer's medium to fragment lysosomes (Perou and Kaplan, 1993; Durchfort et al., 2012). After the removal of Ringer's medium, lysosome sizes were tracked by flow cytometry to monitor their fusion activity (Fig. 2*A*). There was no significant difference in the rate of lysosome size increase between *Fig4* $^{+/+}$ and *Fig4* $^{-/-}$ fibroblasts (Fig. 2*A*,*B*).

We then tested lysosomal fission. Fibroblasts were treated with vacuolin-1 to increase lysosome size (Fig. 2*C*). After removal of vacuolin-1, lysosome sizes were measured by flow cytometry to track their fission activity. By the 15th hour, the size of lysosomes reached an 83% recovery in *Fig4* $^{+/+}$ cells, versus a 37% recovery in *Fig4* $^{-/-}$ cells.

One might be concerned about large lysosomes being fractured during homogenization of the cells, leading to an underestimation of lysosome sizes in *Fig4* $^{-/-}$ cells. We examined the live cells by DIC imaging and counted the percentage of cells with vacuole sizes more than one-third of the nuclear diameter. A strong recovery was evident in *Fig4* $^{+/+}$ cells. However, lysosomes in *Fig4* $^{-/-}$ cells were further enlarged even after withdrawal of vacuolin-1 and showed no recovery (Fig. 2*D*).

Together, these results demonstrate that FIG4 deficiency selectively impairs lysosomal fission but spares lysosomal fusion. This mechanism explains abnormal lysosomal storage in *Fig4* $^{-/-}$ cells.

High Ca^{2+} levels in $Fig4^{-/-}$ lysosomes

To understand how lysosomal fission is impaired in *Fig4*$^{-/-}$ cells, we explored intralysosomal Ca^{2+} levels since this change has been involved in lysosomal storage (Lloyd-Evans and Platt, 2011). Moreover, $PI3,5P_2$ is an endogenous ligand of the Ca^{2+} channel TRPML1 located in the lysosomal membrane (Dong et al., 2010). Deficiency of $PI3,5P_2$ in *Fig4*$^{-/-}$ cells is expected to deactivate the TRPML1 channels and suppresses the Ca^{2+} release from *Fig4*$^{-/-}$ lysosomes. We stained the *Fig4*$^{-/-}$ fibroblasts with a Ca^{2+} dye (Calcium Orange; Fig. 3*A*,*B*, red). Ca^{2+} fluorescence intensity was significantly higher in *Fig4*$^{-/-}$ cells than that in *Fig4*$^{+/+}$ fibroblasts (Fig. 3*G*).

Ca^{2+} signals were strong and often masked the dextran signals in *Fig4*$^{-/-}$ cells. There were stronger dextran signals in *Fig4*$^{-/-}$ cells than that in *Fig4*$^{+/+}$ cells (Fig. 3*B*). This was consistent with excessive lysosomal storage in *Fig4*$^{-/-}$ cells. Robust Ca^{2+} signals were clearly visible in individual vacuoles of lysosome (Fig. 3*B*). Therefore, higher Ca^{2+} levels were the cause for the stronger signals in *Fig4*$^{-/-}$ lysosomes, rather than through an increase in the number of lysosomes. The increase of intralysosomal Ca^{2+} levels was also observed in *Fig4*$^{-/-}$ Schwann cell culture (Fig. 3*C*,*D*), *Fig4*$^{-/-}$ neuron culture (Fig. 3*E*,*F*,*H*), as well as *in vivo* myelinated Schwann cells of *Fig4*$^{-/-}$ mouse sciatic nerves (Fig. 3*I–L*).

Alteration of lysosomal pH may affect the results of the calcium dye. We thus tested the Ca^{2+} levels in Schwann cell cultures using pH-insensitive dye, Oregon Green 488 BAPTA-2-AM (10 μM; Molecular Probes, catalog #06809) (Takahashi et al., 1999). Again, the results demonstrated a significant increase of Ca^{2+} level in *Fig4*$^{-/-}$ cells (50.6 ± 19.9 gray values/μM^2 in 51 *Fig4*$^{-/-}$ cells vs 24.1 ± 10.0 gray values/μM^2 in 42 *Fig4*$^{+/+}$ cells; $p < 0.001$).

Moreover, we have examined the Ca^{2+} sources in Schwann cells by using a culture medium either free of Ca^{2+} or added with 1.8 mM Ca^{2+}. Schwann cells were incubated with media for 2 h. The cells were then stained with a calcium dye, Oregon Green, and imaged as described in Materials and Methods. Ca^{2+} fluorescent intensity was not significantly different between *Fig4*$^{-/-}$ cells with Ca^{2+}-free medium and *Fig4*$^{-/-}$ cells with Ca^{2+}-added medium (208.1 ± 62.6 gray values/μM^2 for Ca^{2+}-added medium vs 191.4 ± 51.5 gray values/μM^2 for Ca^{2+}-free medium; 70 cells from 20 fields under 63× lens or 100 cells from 19 fields under 63× lens respectively; $p > 0.05$). In addition, using the patch-clamp technique, Ca^{2+} influx across cytoplasmic membrane store-operated Ca^{2+} channels (conducting extracellular Ca^{2+} to intracellular endoplasmic reticulum) was evaluated in immortalized Schwann cells and showed no difference between *Fig4*$^{+/+}$ and *Fig4*$^{-/-}$ cells (Fig. 4). Finally, we performed Western blot with pan-voltage-gated Ca^{2+} channel antibodies to compare the Ca^{2+} channel levels at cellular membrane between *Fig4*$^{+/+}$ and *Fig4*$^{-/-}$ mouse sciatic nerves. Again, there was no difference between the two types of cells (data not shown).

To further substantiate the intralysosomal localization of Ca^{2+}, we transfected Schwann cells using the BacMam vector 2.0 (Invitrogen; catalog #C10597) to express a red fluorescence pro-

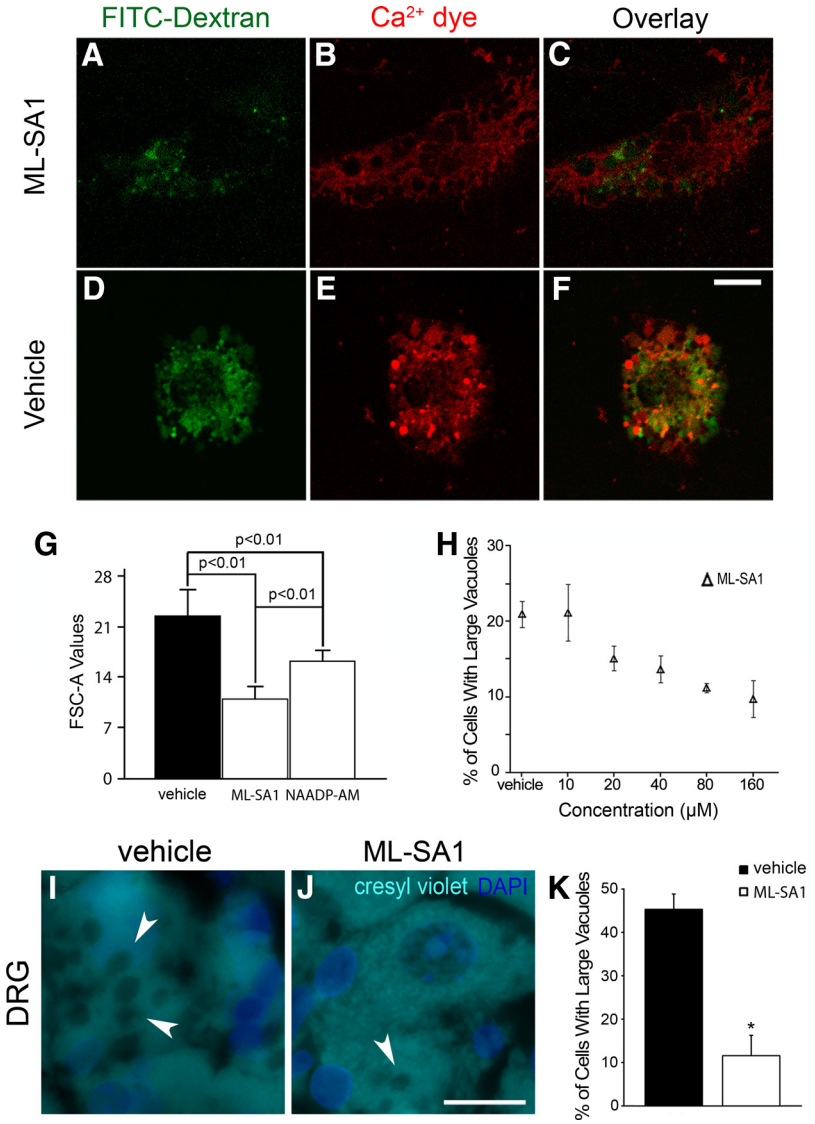

Figure 5. High intralysosomal Ca^{2+} level and abnormal lysosomal storage in *Fig4*$^{-/-}$ cells are rescued by pharmacologically activating TRPML1 channels. TRPML1 ligand, ML-SA1 (20 μM), was applied to activate TRPML1 channels in fibroblast culture for 30 min. ***A–F***, Lysosomes were labeled with FITC-dextran (green). Ca^{2+} was revealed by calcium orange (red). Ca^{2+} was mainly distributed in the lysosome. ML-SA1 treatment reduced the Ca^{2+} level in *Fig4*$^{-/-}$ lysosomes. ***G***, Flow cytometry showed that 48 h incubation with ML-SA1 decreased the lysosome sizes by 50% of that in the vehicle group ($n = 4$ sets of cultures; $p < 0.01$). NAADP-AM (1 μM) reduced lysosome sizes by 27%, compared with that in the vehicle group ($n = 4$ sets of cultures; $p < 0.01$). ***H***, The percentage of cells with large vacuoles (more than one-third of nuclear diameter) was counted. ML-SA1 produced a dose-dependent response in reducing lysosome sizes. ***I***, Paraffin sections of *Fig4*$^{-/-}$ mouse DRG were stained with cresyl violet and imaged under fluorescence microscopy. The DRGs incubated with vehicle (DMSO) for 36 h showed numerous vacuoles (arrowheads) in neuronal cytoplasm. ***J***, The same preparation of mouse DRGs treated with ML-SA1 (40 μM) for 36 h showed only a few neurons containing small vacuoles. Scale bar, 10 μm. ***K***, The percentage of neurons with vacuoles were manually counted and showed a significant reduction of vacuolated neurons in ML-SA1-treated DRGs (12 ± 5%; $n = 4$ mice), compared with that in vehicle-treated DRGs (45 ± 3%; $n = 4$ mice; $p < 0.01$; 346 neurons counted in vehicle group and 438 neurons counted in ML-SA1 group). Asterisks (*) indicate statistically significant.

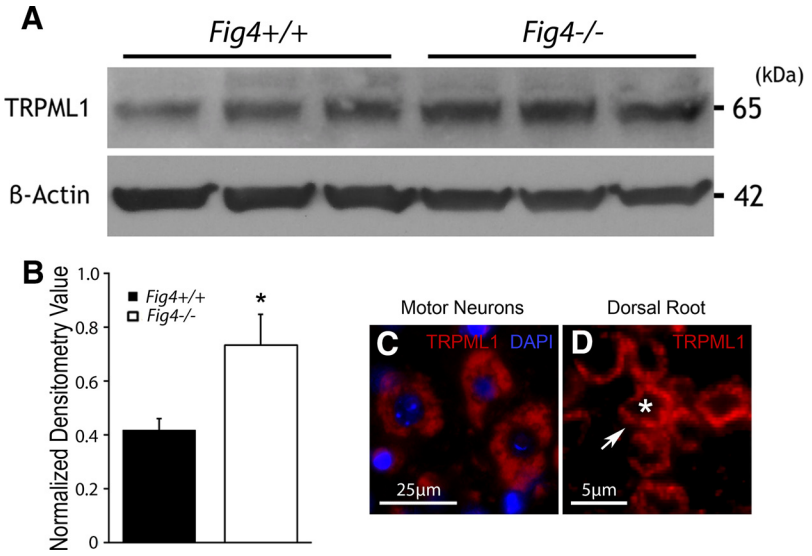

Figure 6. TRPML1 expression in fibroblasts and nervous system. ***A***, TRPML1 levels in $Fig4^{+/+}$ and $Fig4^{-/-}$ fibroblasts were quantified by Western blot. ***B***, Densitometry showed a significant increase of TRPML1 in $Fig4^{-/-}$ fibroblasts (0.73 ± 0.11), compared with that in $Fig4^{+/+}$ fibroblasts (0.42 ± 0.04; $n = 3$ cultures; $p < 0.01$). The specificity of TRPML1 antibody was verified in mutant human fibroblasts with no TRPML1 expression (data not shown). ***C***, TRPML1 was stained in paraffin sections of $Fig4^{+/+}$ spinal cord (red). TRPML1 immunoreactivity was found in the cytoplasm of spinal motor neurons. ***D***, The same staining was done in $Fig4^{+/+}$ spinal roots. TRPML1 was found in the myelin (arrow) but absent in axons (*). The pattern of TRPML1 distribution in $Fig4^{-/-}$ tissues was comparable with that in $Fig4^{+/+}$ tissues.

tein (RFP)-fused LAMP1, a lysosomal transmembrane protein. This specifically labeled the outer margin of lysosomes (Fig. 3*M*). More importantly, this allowed us to clearly visualize the lysosomal lumen in the enlarged lysosomes of $Fig4^{-/-}$ cells. When these cells were double-labeled with the calcium dye, Oregon Green, Ca^{2+} were unequivocally localized within the lumen of lysosomes (Fig. 3*M*). Together, an abnormal Ca^{2+} increase was mainly in the lysosomes and was an abnormality common to all types of $Fig4^{-/-}$ cells.

High intralysosomal Ca^{2+} level and abnormal lysosomal storage are rescued by pharmacologically activating TRPML1 channels

The high intralysosomal Ca^{2+} level in $Fig4^{-/-}$ cells is highly relevant to abnormal lysosomal storage because autosomal recessive mutations in human *TRPML1* gene cause a lysosomal storage disease, called mucolipidosis Type IV (Cox and Cachón-González, 2012). Thus, it is reasonable to speculate that the high level of intralysosomal Ca^{2+} by FIG4/PI3,5P_2 deficiency can be reversed by application of a previously established synthetic TRPML1 ligand, ML-SA1 (Dong et al., 2010; Samie et al., 2013). Indeed, application of ML-SA1 reduced the level of intralysosomal Ca^{2+} (Fig. 5*A–F*).

Because ablation of *Trpml1* in mice induced abnormal lysosomal storage (Venugopal et al., 2007), reactivation of TRPML1 by ML-SA1 is expected to improve lysosomal storage in $Fig4^{-/-}$ cells. In addition, the excessive Ca^{2+} may be released by activating another lysosomal Ca^{2+} channel, TPC2, through application of the TPC2 ligand, NAADP (Pitt et al., 2010). If the high Ca^{2+} level is pathogenic, release of the intralysosomal Ca^{2+} should alleviate the abnormal lysosomal storage in $Fig4^{-/-}$ cells. Lysosome sizes in mouse $Fig4^{-/-}$ fibroblasts were quantified by flow cytometry and compared between treated (20 μM ML-SA1 or 1 μM NAADP-AM; 24 h) and vehicle cells. Both ML-SA1 and NAADP-AM reduced lysosome sizes (Fig. 5*G*). NAADP cannot penetrate the cell membrane; therefore, NAADP was modified to NAADP-AM (acetoxylmethyl) by Vanderbilt Chemical Synthesis Core as described previously (Park et al., 2013). Acetoxylmethylation is a widely used chemical modification to render a compound membrane-permeable. Percentages of fibroblasts with large vacuoles were counted as described in Figure 2*D* to show the dose dependence response to ML-SA1 treatment (Fig. 5*H*).

Next, we tested ML-SA1's therapeutic potential in an *ex vivo* preparation (Fig. 5*I,J*). Spinal cords with attached DRGs from P5 mice ($n = 4$ ML-SA1-treated $Fig4^{-/-}$ mice and $n = 4$ vehicle-treated $Fig4^{-/-}$ mice) were treated with either vehicle (DMSO) or ML-SA1 (40 μM) for 36 h. We counted percentages of neurons with vacuoles (Fig. 5*K*). There was a significant decrease of vacuolated neurons (Fig. 5*I,J*, arrowheads) in ML-SA1-treated DRGs (12 ± 5%), compared with that in vehicle-treated DRGs (45 ± 3%; $n = 4$ mice; $p < 0.01$; 346 cells counted in vehicle group and 438 cells counted in ML-SA1 group).

These data together suggest that the high Ca^{2+} level in $Fig4^{-/-}$ cells is predominantly present in lysosomes. This likely resulted from deactivation of TRPML1 channels when PI3,5P_2 is deficient. Activation of these TRPML1 Ca^{2+} channels pharmacologically rescues the abnormal lysosomal storage in both cell culture and *ex vivo* nervous tissues, supporting a pathogenic role of high Ca^{2+} levels in $Fig4^{-/-}$ lysosomes.

TRPML1 is expressed in the peripheral nervous system and increased in $Fig4^{-/-}$ fibroblasts

Lysosomal fission defect could also be contributed by a downregulation of TRPML1 (the receptor of PI3,5P_2) in $Fig4^{-/-}$ cells. However, Western blot revealed an increase, not decrease, of TRPML1 protein level in $Fig4^{-/-}$ fibroblasts (0.73 ± 0.11) compared with that in $Fig4^{+/+}$ fibroblasts (0.42 ± 0.04; $n = 3$ assays; $p < 0.05$; Fig. 6*A,B*). This increase is presumably due to an overall increase of lysosomal membrane proteins in $Fig4^{-/-}$ mice (Katona et al., 2011).

To delineate expression of TRPML1 in the nervous system, we performed immunostaining of mouse tissues with antibodies against TRPML1. TRPML1 was detected in the neuronal cell body of spinal cords (Fig. 6*C*). TRPML1 was also expressed in myelin but absent in axons of peripheral nerves (Fig. 6*D*, asterisk). The pattern of TRPML1 localization appeared to be comparable between $Fig4^{-/-}$ and $Fig4^{+/+}$ nerve tissues.

Suppressed Ca^{2+} efflux from $Fig4^{-/-}$ lysosomes impairs lysosomal fission by downregulating dynamin-1 expression/activity

To understand how the high intralysosomal Ca^{2+} level affects lysosomal fission, we investigated dynamin, a calcium-sensitive GTPase that is known to play key roles in endoplasmic reticulum fission by scissoring the budding vesicles (Sweitzer and Hinshaw, 1998; Stowell et al., 1999). A recent study has demonstrated that dynamin is required for *lysosomal* fission (Schulze et al., 2013).

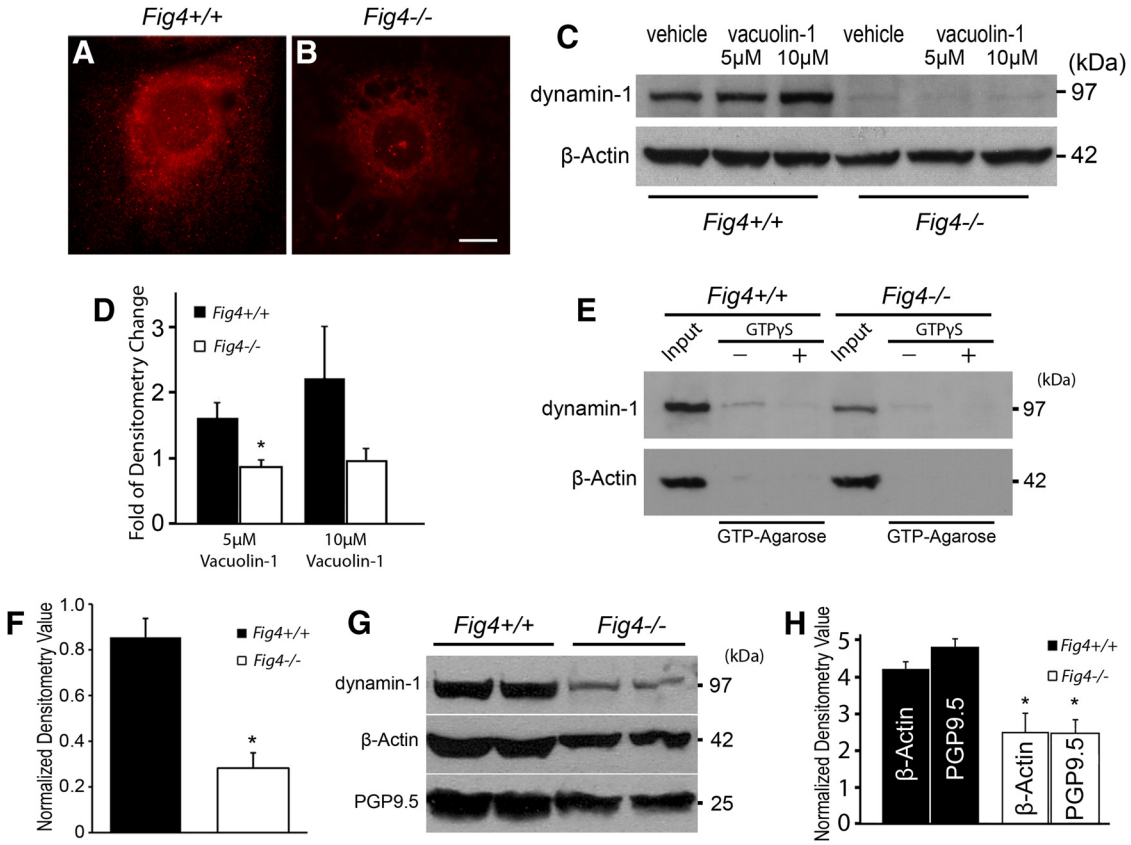

Figure 7. Downregulation of dynamin-1 in *Fig4*$^{-/-}$ cells. ***A***, ***B***, Fibroblasts were stained for dynamin-1 (red). There appeared to be a decrease of dynamin-1 immunoreactivity in *Fig4*$^{-/-}$ fibroblasts, compared with that in *Fig4*$^{+/+}$ fibroblasts. Scale bar, 10 μm. ***C***, Western blot showed a severely decreased dynamin-1 level in *Fig4*$^{-/-}$ fibroblasts, compared with that in *Fig4*$^{+/+}$ fibroblasts. Vacuolin-1 treatment raised the dynamin-1 level in *Fig4*$^{+/+}$ fibroblasts but exerted no effect on the dynamin-1 level in *Fig4*$^{-/-}$ fibroblasts. ***D***, Dynamin-1 levels were quantified by densitometry of Western blot. Fold increase by vacuolin-1 (5 or 10 μM) treatment over the level of vehicle was plotted in the histogram. It showed a statistically significant decrease of dynamin-1 in *Fig4*$^{-/-}$ fibroblasts at 5 μM vacuolin-1 ($n = 3$ assays for each group). *Statistically significant ($p < 0.01$). The 10 μM vacuolin-1 induced a trend of dynamin-1 increase but did not reach a statistical significance due to large variations. ***E***, GTP activity assay was performed as described in Materials and Methods. Dynamin-1 GTPase activity was present in *Fig4*$^{+/+}$ fibroblasts but hardly visible in *Fig4*$^{-/-}$ fibroblasts. ***F***, Densitometry quantification confirmed a significant decrease of dynamin-1 level in *Fig4*$^{-/-}$ fibroblast (0.85 ± 0.08), compared with that in *Fig4*$^{+/+}$ fibroblasts (0.28 ± 0.07; $n = 5$ assays for each group; $p < 0.01$). ***G***, Proteins from P21 mouse brains were evaluated by Western blot. β-Actin was used as loading controls. Neuron-specific protein PGP9.5 was used as additional control. ***H***, Densitometry showed a significant decrease of dynamin-1 levels in *Fig4*$^{-/-}$ brains (2.5 ± 0.52), compared with that in *Fig4*$^{+/+}$ brains (4.2 ± 0.17; $n = 3$ mice; $p < 0.01$; normalized by β-actin). The comparison was also made after the dynamin-1 levels were normalized by PGP9.5. It also showed a significant decrease in *Fig4*$^{-/-}$ brains (2.5 ± 0.42), compared with that in *Fig4*$^{+/+}$ brains (4.9 ± 0.25; $n = 3$ mice; $p < 0.01$). Asterisks (*) indicate statistically significant.

Because dynamin is activated by calcium, we hypothesize that the lysosomal fission defect in *Fig4*$^{-/-}$ cells is due to impaired dynamin function.

Downregulation of dynamin-1 expression/activity in Fig4$^{-/-}$ *cells*

Immunostaining was used to detect dynamin-1 in *Fig4*$^{+/+}$ and *Fig4*$^{-/-}$ fibroblasts. There appeared to be higher levels of dynamin-1 in *Fig4*$^{+/+}$ cytoplasm than in *Fig4*$^{-/-}$ cytoplasm (Fig. 7*A*,*B*). This difference was confirmed by Western blot in the vehicle lanes of Figure 7*C* and the input lanes of Figure 7*E* (0.28 ± 0.07 in *Fig4*$^{-/-}$ cells vs 0.85 ± 0.08 in *Fig4*$^{+/+}$ cells; $n = 5$ assays; $p < 0.01$).

To determine whether the difference of dynamin-1 expression is associated with a difference of dynamin-1 GTPase activity, we performed a GTPase activity assay by modifying a published method (Zhang et al., 2013). GTPase activity was present in *Fig4*$^{+/+}$ fibroblasts but hardly detectable in *Fig4*$^{-/-}$ fibroblasts (Fig. 7*E*). However, the ratio between activated GTPase level and total dynamin-1 level was not significantly different between *Fig4*$^{+/+}$ ($5.6 \pm 1.1\%$) and *Fig4*$^{-/-}$ cells ($5.9 \pm 1.0\%$; $n = 3$ assays; $p = 0.69$). Therefore, the reduction of dynamin-1 activity in *Fig4*$^{-/-}$ cells was mainly attributed to the decrease of total dynamin-1 expression.

Failure of expressing dynamin-1 in Fig4$^{-/-}$ *cells during the high demand of lysosomal fission*

Vacuolin-1 maximizes lysosome size through an unknown mechanism, which would demand highly active fission to restore the lysosomal sizes after the removal of vacuolin-1. We speculated that vacuolin-1 will raise the level of dynamin-1 in *Fig4*$^{+/+}$ cells, but *Fig4*$^{-/-}$ cells may not respond to the vacuolin-1 stimuli. *Fig4*$^{+/+}$ fibroblasts were treated with vacuolin-1 (5 or 10 μM for 1 h) to enlarge lysosomes. Cell lysates were collected for Western blot at 4 h after the removal of vacuolin-1 when lysosomal fission became highly active (Fig. 2*D*). There was a significant increase of dynamin-1 levels in *Fig4*$^{+/+}$ cells. However, this increase of dynamin-1 was not seen in *Fig4*$^{-/-}$ cells after treatment with the vacuolin-1 (Fig. 7*C*,*D*).

To further determine the role of dynamin-1 in lysosomal fission, we have used dynasore, a specific dynamin-GTPase inhibitor (Fig. 8). Following a 1 h treatment of 10 μM vacuolin-1, lysosomes in wild-type fibroblasts reached their peak size around

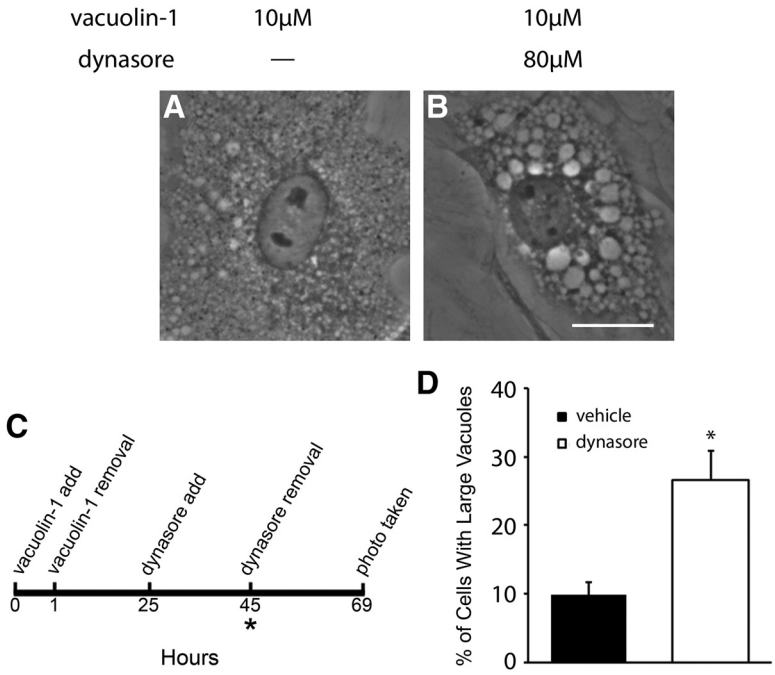

Figure 8. ***A***, ***B***, Dynamin-1 is involved in lysosomal fission. Fig4 $^{+/+}$ fibroblasts were treated with vacuolin-1 (10 μM) for1 h. Cells were kept at 37°C for 24 h to reach maximal lysosome size. Dynasore (80 μM) was added at the 25th hour for 20 h. Cells were imaged at the 69th hour to observe vacuoles. ***C***, Application of the drugs is marked in a time line. *Time point when there was a transient decrease of lysosome size for unknown reason. ***D***, The percentage of cells with large vacuoles (more than one-third of nuclear diameter) was counted (26 ± 4% in dynasore group vs 10 ± 2% in vehicle group; $p < 0.01$; $n = 6$ cultures; >200 cells counted).

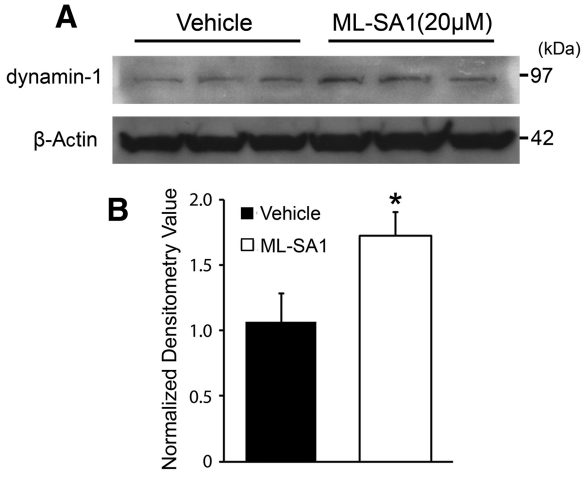

Figure 9. Reversal of dynamin-1 level by treatment of ML-SA1. ***A***, *Fig4* $^{-/-}$ fibroblasts were treated with ML-SA1 (20 μM) or vehicle overnight, followed by Western blot to quantify the dynamin-1 level. Results were normalized by β-actin. ***B***, Densitometry showed a significant increase of dynamin-1 level in ML-SA1-treated fibroblasts (1.7 ± 0.2), compared with that in vehicle-treated fibroblasts (1.1 ± 0.2; $n = 6$ assays; $p < 0.01$). Asterisks (*) indicate statistically significant.

the 24th hour. After this point, lysosomal fission activity was expected to be high. Dynasore was added at the 25th hour to block lysosomal fission. All cells were imaged at the 69th hour and counted as described in Figure 2*D*. The percentage of cells with large vacuoles was 26 ± 4% in dynasore-treated fibroblasts but was only 10 ± 2% in vehicle-treated fibroblasts ($n = 3$ experiments; >50 cell counted in each experiment; $p < 0.01$; Fig. 8*D*). These data suggest that dynamin activity regulates fission of wild-type lysosomes.

The reduced dynamin-1 level is reversed by reactivation of lysosomal TRPML1 Ca^{2+} channel

We speculated that the reduction of dynamin-1 expression in *Fig4* $^{-/-}$ cells is related to the inactivation of Ca^{2+} efflux through lysosomal TRPML1 channels. We treated *Fig4* $^{-/-}$ fibroblasts with or without ML-SA1, followed by Western blot to quantify the dynamin-1 level. The results showed a significant increase of dynamin-1 in cells treated with ML-SA1 (1.7 ± 0.2), compared with that in vehicle-treated cells (1.1 ± 0.2; $n = 6$; $p < 0.01$; Fig. 9*A*,*B*). This finding suggests that suppressed Ca^{2+} efflux from lysosomes is one of the mechanisms responsible for the decreased dynamin-1 expression in *Fig4* $^{-/-}$ cells.

Dynamin-1 expression is also decreased in Fig4 $^{-/-}$ *mouse brain*

To determine whether the mechanism of dynamin-1 reduction is pathogenically relevant *in vivo*, we have performed Western blot in *Fig4* $^{+/+}$ and *Fig4* $^{-/-}$ mouse brains at P21 d of age. There was a significant difference of dynamin-1 level between *Fig4* $^{-/-}$ and *Fig4* $^{+/+}$ mouse brains (4.2 ± 0.2; $n = 3$ *Fig4* $^{+/+}$ mice vs 2.5 ± 0.5; $n = 3$ *Fig4* $^{-/-}$ mice; $p < 0.01$; Fig. 7*G*,*H*). The reduction of dynamin-1 could be secondary to the neuronal loss in *Fig4* $^{-/-}$ brains. To exclude this possibility, dynamin-1 levels were normalized by the neuronal marker PGP9.5. There was still a significant decrease of dynamin-1 in *Fig4* $^{-/-}$ brains, compared with that in *Fig4* $^{+/+}$ brains. Moreover, the difference of dynamin-1 levels was replicated in P5 mouse brains, when neurodegeneration starts (3.7 ± 0.2 for 3 *Fig4* $^{+/+}$ mouse brains vs 2.7 ± 0.2 for 3 *Fig4* $^{-/-}$ mouse brains; $p < 0.01$).

Together, data both *in vitro* and *in vivo* suggest that inactivation of TRPML1 Ca^{2+} channels downregulates dynamin-1 expression, thereby leading to the impaired fission and abnormal storage of lysosomes.

Discussion

Although $PI3,5P_2$ has been proposed to be involved in lysosomal membrane trafficking for a long time, it is still unknown how $PI3,5P_2$ deficiency affects lysosomal trafficking in diseases with FIG4 deficiency. Our study demonstrates a fission defect of lysosomes in *Fig4* $^{-/-}$ cells. This finding explains abnormal lysosomal storage in FIG4-deficient human cells and mouse model (Chow et al., 2007; Zhang et al., 2008; Katona et al., 2011; Martyn and Li, 2013). This novel mechanism is in line with our time-lapse imaging study showing a decrease of budding vesicles in FIG4-deficient human fibroblasts (Zhang et al., 2008).

We further show that defective lysosomal fission is likely caused by a robust increase of intralysosomal Ca^{2+} level in *Fig4* $^{-/-}$ cells. This mechanism is consistent with the known biology of TRPML1. This hexa-span membrane protein forms Ca^{2+} channels in the lysosomal membrane with both N- and C-terminals in the cytoplasmic side. Several positively charged residues in the N-terminal of TRPML1 allow cytoplasmic $PI3,5P_2$ to bind with TRPML1 with high specificity. This binding pro-

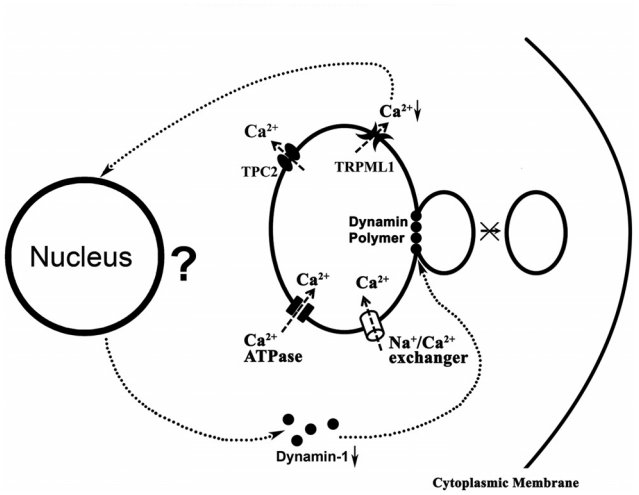

Figure 10. Mechanisms of impaired lysosomal fission in FIG4-deficient cells. This diagram illustrates our hypothetical mechanisms responsible for abnormal lysosomal fission based on data presented in this study. The entry of Ca^{2+} into lysosomes is through Na^{+}/Ca^{2+} exchangers and the Ca^{2+} ATPase pump, whereas release of Ca^{2+} is primarily through two Ca^{2+} channels, TRPML1 and TPC2 (Lloyd-Evans and Platt, 2011). $PI3,5P_2$ binds with TRPML1 to activate Ca^{2+} efflux through TRPML1 (Dong et al., 2010), whereas TPC2 is activated by its ligand NAADP (Pitt et al., 2010). Because $PI3,5P_2$ is deficient in *Fig4*$^{-/-}$ cells, lysosomes develop a high level of Ca^{2+}. The extra Ca^{2+} in *Fig4*$^{-/-}$ lysosomes can be released by application of a TRPML1 synthetic ligand ML-SA1 (Samie et al., 2013) or TPC2 ligand NAADP (Lloyd-Evans and Platt, 2011). Ca^{2+} from lysosomes activates expression of dynamins (via an unknown mechanism) to scissor lysosomal membrane for fission. However, inactivation of TRPML1 channels by FIG4/$PI3,5P_2$ deficiency would block the activation of dynamin expression by preventing Ca^{2+} released from lysosomes.

motes Ca^{2+} efflux through the TRPML1 channels as demonstrated in an elegant patch-clamp study by Dong et al. (2010). Deficiency of $PI3,5P_2$ in FIG4 deficiency would suppress Ca^{2+} efflux from lysosomes. Indeed, application of a synthetic ligand of TRPML1, ML-SA1, rescues lysosomal fission defect and abnormal lysosomal storage in *Fig4*$^{-/-}$ cells. This is also supported by the abnormal lysosomal storage in mice with null of *Trpml1* (Venugopal et al., 2007). Finally, release of intralysosomal Ca^{2+} by activating a different lysosomal Ca^{2+} channel, TPC2, improved lysosomal storage as well. This finding further supports a causal role of intralysosomal Ca^{2+} in abnormal lysosomal storage. This approach is therapeutically significant because application of ML-SA1 reverses lysosomal pathology in *ex vivo* tissues from *Fig4*$^{-/-}$ mice (Fig. 5*I–K*).

Next, a logical question would be how the high intralysosomal Ca^{2+} level suppresses lysosomal fission in FIG4 deficiency. We provide evidence both *in vitro* and *in vivo* that the suppressed Ca^{2+} efflux through TRPML1 channels downregulates the expression of dynamin-1, a GTPase known to regulate fissions of intracellular organelles (Sweitzer and Hinshaw, 1998; Stowell et al., 1999). The finding is pathogenically relevant for the following reasons: (1) Dynamin was significantly decreased in *Fig4*$^{-/-}$ culture cells and *Fig4*$^{-/-}$ mouse brains. (2) The increased demand of lysosomal fission by Vacuolin-1 treatment was able to raise the dynamin level in *Fig4*$^{+/+}$ cells but failed to do so in *Fig4*$^{-/-}$ cells. (3) Application of the dynamin-specific inhibitor Dynasore in *Fig4*$^{+/+}$ cells blocked lysosomal fission. (4) The decrease of dynamin level was reversed by application of lysosomal Ca^{2+} channel TRPML1 activator, ML-SA1. Together, loss of the dynamin scissoring activity in FIG4-deficient cells offers satisfying explanations for the lysosomal fission defect in *Fig4*$^{-/-}$ cells. This finding is consistent with the fact that genetically deletion of *dynamin-1* gene in mice results in drastically increased sizes of lysosomes (Schulze et al., 2013).

How Ca^{2+} activates dynamin-1 remains to be determined. However, calcineurin is a Ca^{2+}-responsive protein that directly binds to dynamin (Cabeza et al., 2010). Ca^{2+} from lysosomes may be required to activate the local dynamin GTPase via calcineurin (Cousin and Robinson, 2000). It also remains to be determined how the efflux of intralysosomal Ca^{2+} regulates expression of dynamin-1.

The lysosome is a recently emerged Ca^{2+} signaling sensor of the cell (Lloyd-Evans and Platt, 2011). This is a remarkable conceptual advance because an increase in intralysosomal Ca^{2+} level has become a common mechanism shared by multiple lysosomal storage diseases (Lloyd-Evans and Platt, 2011; Shen et al., 2012). By targeting this process, an effective therapeutic strategy has been developed against Niemann–Pick disease Type C1 (Lloyd-Evans et al., 2008). Moreover, identification of TRPML1 ligands has provided specific chemical tools to manipulate this system. We now extend this approach to a group of diseases caused by FIG4 deficiency.

TRPML1 synthetic ligands have no binding receptor in mucolipidosis-IV because recessive mutations in *TRPML1* result in no/minimal TRPML1 translated. Even if mutant TRPML1s are translated, they cannot bind with their ligand $PI3,5P_2$ due to the receptor TRPML1 being mutated. Thus, a disease, such as mucolipidosis-IV, offers no therapeutic target for the TRPML1 synthetic ligands (Dong et al., 2010; Wakabayashi et al., 2011). In contrast, diseases with FIG4 deficiency serve as excellent models to test the biological functions of TRPML1/$PI3,5P_2$ interaction in animals and humans. A reversal of lysosomal phenotype by ML-SA1 supports that $PI3,5P_2$ interaction with TRPML1 is a predominant mechanism for abnormal lysosomal storage in FIG4-deficient cells.

Furthermore, the implication of this approach may go beyond FIG4 deficiency. For instance, deficiency of two $PI3,5P_2$ phosphatases, MTMR2 or MTMR13, causes CMT4B1 and CMT4B2, respectively (Bolino et al., 2002). This phosphatase abnormality leads to an increase of $PI3,5P_2$ levels (Vaccari et al., 2011), which would overstimulate TRPML1 channels in CMT4B1 or 4B2. Antagonists of TRPML1 may prove to be a therapeutic approach against these diseases.

Lysosomal storage could be caused by additional mechanisms, such as alteration of lysosomal pH or suppression of protein degradation. In addition, a recent publication shows an autophagic defect in *Fig4*$^{-/-}$ Schwann cells (Vaccari et al., 2015). However, in our hands, defect of autophagy was negligible and was controversial based on other studies (Zhou et al., 2010; Katona et al., 2011; Ferguson et al., 2012; Martyn and Li, 2013). More importantly, all these alternative mechanisms are not mutually exclusive with our proposed mechanism of TRPML1 Ca^{2+} channel suppression.

In conclusion (see Fig. 10), our results revealed a defect of lysosomal fission, but not fusion in FIG4-deficient cells. This defect appears to be caused by a suppression of lysosomal TRPML1 Ca^{2+} channel activity due to the deficiency of the TRPML1 ligand, $PI3,5P_2$. The failure of Ca^{2+} release from *Fig4*$^{-/-}$ lysosomes downregulates the dynamin-1 expression. Because dynamin-1 is required for lysosomal membrane scissoring, deficiency of dynamin-1 in FIG4-deficient cells explains the lysosomal fission defect and abnormal storage of lysosomes. Together with phenotypic reversal by ML-SA1 in *ex vivo* neural tissues, our data offer a potential therapeutic strategy by using TRPML1 synthetic ligands in the diseases with FIG4 deficiency.

References

Bolino A, Marigo V, Ferrera F, Loader J, Romio L, Leoni A, Di Duca M, Cinti R, Cecchi C, Feltri ML, Wrabetz L, Ravazzolo R, Monaco AP (2002) Molecular characterization and expression analysis of Mtmr2, mouse homologue of MTMR2, the Myotubularin-related 2 gene, mutated in CMT4B. Gene 283:17–26. CrossRef Medline

Cabeza JM, Acosta J, Alés E (2010) Dynamics and regulation of endocytotic fission pores: role of calcium and dynamin. Traffic 11:1579–1590. CrossRef Medline

Campeau PM, Lenk GM, Lu JT, Bae Y, Burrage L, Turnpenny P, Román Corona-Rivera J, Morandi L, Mora M, Reutter H, Vulto-van Silfhout AT, Faivre L, Haan E, Gibbs RA, Meisler MH, Lee BH (2013) Yunis-Varon syndrome is caused by mutations in FIG4, encoding a phosphoinositide phosphatase. Am J Hum Genet 92:781–791. CrossRef Medline

Cárdenas AM, Allen DD, Arriagada C, Olivares A, Bennett LB, Caviedes R, Dagnino-Subiabre A, Mendoza IE, Segura-Aguilar J, Rapoport SI, Caviedes P (2002) Establishment and characterization of immortalized neuronal cell lines derived from the spinal cord of normal and trisomy 16 fetal mice, an animal model of Down syndrome. J Neurosci Res 68:46–58. CrossRef Medline

Cerny J, Feng Y, Yu A, Miyake K, Borgonovo B, Klumperman J, Meldolesi J, McNeil PL, Kirchhausen T (2004) The small chemical vacuolin-1 inhibits Ca(2+)-dependent lysosomal exocytosis but not cell resealing. EMBO Rep 5:883–888. CrossRef Medline

Chow CY, Zhang Y, Dowling JJ, Jin N, Adamska M, Shiga K, Szigeti K, Shy ME, Li J, Zhang X, Lupski JR, Weisman LS, Meisler MH (2007) Mutation of FIG4 causes neurodegeneration in the pale tremor mouse and patients with CMT4J. Nature 448:68–72. CrossRef Medline

Cousin MA, Robinson PJ (2000) Ca(2+) influx inhibits dynamin and arrests synaptic vesicle endocytosis at the active zone. J Neurosci 20:949–957. Medline

Cox TM, Cachón-González MB (2012) The cellular pathology of lysosomal diseases. J Pathol 226:241–254. CrossRef Medline

Dong XP, Shen D, Wang X, Dawson T, Li X, Zhang Q, Cheng X, Zhang Y, Weisman LS, Delling M, Xu H (2010) PI(3,5)P(2) controls membrane traffic by direct activation of mucolipin Ca release channels in the endolysosome. Nat Commun 1:38. CrossRef Medline

Durchfort N, Verhoef S, Vaughn MB, Shrestha R, Adam D, Kaplan J, Ward DM (2012) The enlarged lysosomes in beige j cells result from decreased lysosome fission and not increased lysosome fusion. Traffic 13:108–119. CrossRef Medline

Ferguson CJ, Lenk GM, Jones JM, Grant AE, Winters JJ, Dowling JJ, Giger RJ, Meisler MH (2012) Neuronal expression of Fig4 is necessary and sufficient to prevent spongiform neurodegeneration. Hum Mol Genet 21:3525–3534. CrossRef Medline

Hamill OP, Marty A, Neher E, Sakmann B, Sigworth FJ (1981) Improved patch-clamp techniques for high-resolution current recording from cells and cell-free membrane patches. Pflugers Arch 391:85–100. CrossRef Medline

Huotari J, Helenius A (2011) Endosome maturation. EMBO J 30:3481–3500. CrossRef Medline

Ikonomov OC, Sbrissa D, Ijuin T, Takenawa T, Shisheva A (2009) Sac3 is an insulin-regulated phosphatidylinositol 3,5-bisphosphate phosphatase: gain in insulin responsiveness through Sac3 down-regulation in adipocytes. J Biol Chem 284:23961–23971. CrossRef Medline

Jin N, Chow CY, Liu L, Zolov SN, Bronson R, Davisson M, Petersen JL, Zhang Y, Park S, Duex JE, Goldowitz D, Meisler MH, Weisman LS (2008) VAC14 nucleates a protein complex essential for the acute interconversion of PI3P and PI(3,5)P(2) in yeast and mouse. EMBO J 27:3221–3234. CrossRef Medline

Katona I, Zhang X, Bai Y, Shy ME, Guo J, Yan Q, Hatfield J, Kupsky WJ, Li J (2011) Distinct pathogenic processes between Fig4-deficient motor and sensory neurons. Eur J Neurosci 33:1401–1410. CrossRef Medline

Lindau M, Neher E (1988) Patch-clamp techniques for time-resolved capacitance measurements in single cells. Pflugers Arch 411:137–146. CrossRef Medline

Lloyd-Evans E, Platt FM (2011) Lysosomal Ca(2+) homeostasis: role in pathogenesis of lysosomal storage diseases. Cell Calcium 50:200–205. CrossRef Medline

Lloyd-Evans E, Morgan AJ, He X, Smith DA, Elliot-Smith E, Sillence DJ, Churchill GC, Schuchman EH, Galione A, Platt FM (2008) Niemann-Pick disease type C1 is a sphingosine storage disease that causes deregulation of lysosomal calcium. Nat Med 14:1247–1255. CrossRef Medline

Luzio JP, Pryor PR, Bright NA (2007) Lysosomes: fusion and function. Nat Rev Mol Cell Biol 8:622–632. CrossRef Medline

Martyn C, Li J (2013) Fig4 deficiency: a newly emerged lysosomal storage disorder? Prog Neurobiol 101:35–45. CrossRef Medline

Mignen O, Shuttleworth TJ (2001) Permeation of monovalent cations through the noncapacitative arachidonate-regulated Ca^{2+} channels in HEK293 cells: comparison with endogenous store-operated channels. J Biol Chem 276:21365–21374. CrossRef Medline

Nicholson G, Lenk GM, Reddel SW, Grant AE, Towne CF, Ferguson CJ, Simpson E, Scheuerle A, Yasick M, Hoffman S, Blouin R, Brandt C, Coppola G, Biesecker LG, Batish SD, Meisler MH (2011) Distinctive genetic and clinical features of CMT4J: a severe neuropathy caused by mutations in the PI(3,5)P2 phosphatase FIG4. Brain 134:1959–1971. CrossRef Medline

Park KH, Kim BJ, Shawl AI, Han MK, Lee HC, Kim UH (2013) Autocrine/paracrine function of NAADP for glucose homeostasis in pancreatic beta cells and adipocytes. J Biol Chem 288:35548–35558. CrossRef Medline

Perou CM, Kaplan J (1993) Chediak-Higashi syndrome is not due to a defect in microtubule-based lysosomal mobility. J Cell Sci 106:99–107. Medline

Perou CM, Leslie JD, Green W, Li L, Ward DM, Kaplan J (1997) The Beige/Chediak-Higashi syndrome gene encodes a widely expressed cytosolic protein. J Biol Chem 272:29790–29794. CrossRef Medline

Pitt SJ, Funnell TM, Sitsapesan M, Venturi E, Rietdorf K, Ruas M, Ganesan A, Gosain R, Churchill GC, Zhu MX, Parrington J, Galione A, Sitsapesan R (2010) TPC2 is a novel NAADP-sensitive Ca^{2+} release channel, operating as a dual sensor of luminal pH and Ca^{2+}. J Biol Chem 285:35039–35046. CrossRef Medline

Saavedra JT, Wolterman RA, Baas F, ten Asbroek AL (2008) Myelination competent conditionally immortalized mouse Schwann cells. J Neurosci Methods 174:25–30. CrossRef Medline

Samie M, Wang X, Zhang X, Goschka A, Li X, Cheng X, Gregg E, Azar M, Zhuo Y, Garrity AG, Gao Q, Slaugenhaupt S, Pickel J, Zolov SN, Weisman LS, Lenk GM, Titus S, Bryant-Genevier M, Southall N, Juan M, et al. (2013) A TRP channel in the lysosome regulates large particle phagocytosis via focal exocytosis. Dev Cell 26:511–524. CrossRef Medline

Sbrissa D, Ikonomov OC, Fu Z, Ijuin T, Gruenberg J, Takenawa T, Shisheva A (2007) Core protein machinery for mammalian phosphatidylinositol 3,5-bisphosphate synthesis and turnover that regulates the progression of endosomal transport: novel Sac phosphatase joins the ArPIKfyve-PIKfyve complex. J Biol Chem 282:23878–23891. CrossRef Medline

Schulze RJ, Weller SG, Schroeder B, Krueger EW, Chi S, Casey CA, McNiven MA (2013) Lipid droplet breakdown requires dynamin 2 for vesiculation of autolysosomal tubules in hepatocytes. J Cell Biol 203:315–326. CrossRef Medline

Shen D, Wang X, Li X, Zhang X, Yao Z, Dibble S, Dong XP, Yu T, Lieberman AP, Showalter HD, Xu H (2012) Lipid storage disorders block lysosomal trafficking by inhibiting a TRP channel and lysosomal calcium release. Nat Commun 3:731. CrossRef Medline

Stowell MH, Marks B, Wigge P, McMahon HT (1999) Nucleotide-dependent conformational changes in dynamin: evidence for a mechanochemical molecular spring. Nat Cell Biol 1:27–32. CrossRef Medline

Sweitzer SM, Hinshaw JE (1998) Dynamin undergoes a GTP-dependent conformational change causing vesiculation. Cell 93:1021–1029. CrossRef Medline

Takahashi A, Camacho P, Lechleiter JD, Herman B (1999) Measurement of intracellular calcium. Physiol Rev 79:1089–1125. Medline

Vaccari I, Dina G, Tronchère H, Kaufman E, Chicanne G, Cerri F, Wrabetz L, Payrastre B, Quattrini A, Weisman LS, Meisler MH, Bolino A (2011) Genetic interaction between MTMR2 and FIG4 phospholipid phosphatases involved in Charcot-Marie-Tooth neuropathies. PLoS Genet 7:e1002319. CrossRef Medline

Vaccari I, Carbone A, Previtali SC, Mironova YA, Alberizzi V, Noseda R, Rivellini C, Bianchi F, Del Carro U, D'Antonio M, Lenk GM, Wrabetz L, Giger RJ, Meisler MH, Bolino A (2015) Loss of Fig4 in both Schwann cells and motor neurons contributes to CMT4J neuropathy. Hum Mol Genet 24:383–396. CrossRef Medline

Venugopal B, Browning MF, Curcio-Morelli C, Varro A, Michaud N, Nanthakumar N, Walkley SU, Pickel J, Slaugenhaupt SA (2007) Neurologic, gastric, and opthalmologic pathologies in a murine model of mucolipidosis type IV. Am J Hum Genet 81:1070–1083. CrossRef Medline

Wakabayashi K, Gustafson AM, Sidransky E, Goldin E (2011) Mucolipidosis type IV: an update. Mol Genet Metab 104:206–213. CrossRef Medline

Walch E, Schmidt M, Brenner RE, Emons D, Dame C, Pontz B, Wiestler OD, Bartmann P (2000) Yunis-Varon syndrome: evidence for a lysosomal storage disease. Am J Med Genet 95:157–160. CrossRef Medline

Yan JG, Matloub HS, Yan Y, Agresti M, Zhang LL, Jaradeh SS (2010) The correlation between calcium absorption and electrophysiological recovery in crushed rat peripheral nerves. Microsurgery 30:138–145. CrossRef Medline

Zhang K, Fishel Ben Kenan R, Osakada Y, Xu W, Sinit RS, Chen L, Zhao X, Chen JY, Cui B, Wu C (2013) Defective axonal transport of Rab7 GTPase results in dysregulated trophic signaling. J Neurosci 33:7451–7462. CrossRef Medline

Zhang X, Chow CY, Sahenk Z, Shy ME, Meisler MH, Li J (2008) Mutation of FIG4 causes a rapidly progressive, asymmetric neuronal degeneration. Brain 131:1990–2001. CrossRef Medline

Zhou X, Wang L, Hasegawa H, Amin P, Han BX, Kaneko S, He Y, Wang F (2010) Deletion of PIK3C3/Vps34 in sensory neurons causes rapid neurodegeneration by disrupting the endosomal but not the autophagic pathway. Proc Natl Acad Sci U S A 107:9424–9429. CrossRef Medline